Macrophages impede CD8 T cells from reaching tumor cells and limit the efficacy of anti–PD-1 treatment

Elisa Peranzoni, Jean Lemoine, Lene Vimeux, Vincent Feuillet, Sarah Barrin, Chahrazade Kantari-Mimoun, Nadège Bercovici, Marion Guérin, Jérôme Biton, Hanane Ouakrim, et al.

Macrophages impede CD8 T cells from reaching tumor cells and limit the efficacy of anti–PD-1 treatment

Elisa Peranzoni[a,b,c,1,2], Jean Lemoine[a,b,c], Lene Vimeux[a,b,c], Vincent Feuillet[a,b,c], Sarah Barrin[a,b,c], Chahrazade Kantari-Mimoun[a,b,c], Nadège Bercovici[a,b,c], Marion Guérin[a,b,c], Jérôme Biton[d], Hanane Ouakrim[d,e], Fabienne Régnier[a,b,c], Audrey Lupo[d,e], Marco Alifano[f], Diane Damotte[d,e], and Emmanuel Donnadieu[a,b,c,2]

[a]INSERM, U1016, Institut Cochin, 75014 Paris, France; [b]CNRS, UMR8104, 75014 Paris, France; [c]Université Paris Descartes, Sorbonne Paris Cité, 75014 Paris, France; [d]INSERM U1138, Cordeliers Research Center, Team Cancer, Immune Control and Escape, University Pierre and Marie Curie, 75006 Paris, France; [e]Department of Pathology, Paris Centre University Hospitals, University Paris Descartes, INSERM U1138, 75006 Paris, France; and [f]Department of Thoracic Surgery, Paris Centre University Hospitals, Université Paris Descartes, 75014 Paris, France

Edited by Douglas T. Fearon, Cornell University, Cambridge, United Kingdom, and approved March 19, 2018 (received for review December 2, 2017)

In a large proportion of cancer patients, CD8 T cells are excluded from the vicinity of cancer cells. The inability of CD8 T cells to reach tumor cells is considered an important mechanism of resistance to cancer immunotherapy. We show that, in human lung squamous-cell carcinomas, exclusion of CD8 T cells from tumor islets is correlated with a poor clinical outcome and with a low lymphocyte motility, as assessed by dynamic imaging on fresh tumor slices. In the tumor stroma, macrophages mediate lymphocyte trapping by forming long-lasting interactions with CD8 T cells. Using a mouse tumor model with well-defined stromal and tumor cell areas, macrophages were depleted with PLX3397, an inhibitor of colony-stimulating factor-1 receptor (CSF-1R). Our results reveal that a CSF-1R blockade enhances CD8 T cell migration and infiltration into tumor islets. Although this treatment alone has minor effects on tumor growth, its combination with anti–PD-1 therapy further increases the accumulation of CD8 T cells in close contact with malignant cells and delays tumor progression. These data suggest that the reduction of macrophage-mediated T cell exclusion increases tumor surveillance by CD8 T cells and renders tumors more responsive to anti–PD-1 treatment.

cancer | immunotherapy | T cells | macrophages | migration

CD8 T cells are key players in the fight against cancer. To kill tumor cells, T cells need to fulfill several functions. First, they should accumulate in the tumor and then migrate efficiently to make a physical contact with malignant cells. Second, they should respond adequately to tumor antigens and to activation signals from other cells. In cancer patients, T cells present several dysfunctions, and current immunotherapy strategies aim mainly at relieving the brake of T cell suppression (1, 2). Whereas some patients exhibit complete and durable tumor regression, in the large majority of individuals these treatments are not effective. The identification of additional barriers preventing T cells from killing tumor cells is a major challenge to achieving more efficient treatments.

There is more and more evidence that defective T cell migration into and within tumors constitutes a resistance mechanism to cancer immunotherapy (3). So far, a lot of attention has been paid to alterations in the entry of T cells into tumors. We know, for example, that tumor blood vessels are abnormal, with reduced expression of chemokines and adhesion molecules, limiting T cells for entering into malignant tissues (4). Nevertheless, the entry of T cells is important but not sufficient to induce tumor regression, as T lymphocytes need to actively scan the tumor tissue to find their targets. Of note, carcinomas are composed of two defined and different regions, namely the tumor islets and a surrounding stroma, enriched in extracellular matrix (ECM) proteins, fibroblasts, blood vessels, and immune cells. Once T cells enter the tumor stroma from the blood, they must navigate within this complex environment before reaching tumor cells.

Accumulating evidence suggests that the total number of T cells found within a tumor, as well as their distribution and ability to localize within tumor islets, are key factors that influence the outcome of tumor development and the responsiveness to cancer immunotherapy. For example, in melanoma patients treated with anti–PD-1 antibodies, the few responding tumors are characterized by the presence of CD8 T cells in the core of the tumor in contact with malignant cells (5). Conversely, patients who do not respond to anti–PD-1 antibodies present pretreatment tumors that either are devoid of T cells or have T cells preferentially located around tumor cell regions, a profile termed "immune-excluded." This default in CD8 T cell–tumor cell interaction has also been observed in other tumors including lung, pancreatic, and ovarian carcinomas and constitutes a major issue for current cancer immunotherapy (6). Thus, there is a great interest in elucidating the mechanisms underlying the recruitment, distribution, and migration of CD8 T cells in tumors. Studies performed over the past few years have increased our understanding of T cell motility processes occurring in various tissues. Both cell-intrinsic and external events play key roles (7, 8). Among the environmental factors that govern the T cell interstitial migration, one has to distinguish the physical structures of the tissue, provided mainly by ECM fibers, the cellular composition

Significance

Cancer immunotherapy is a promising therapeutic intervention. However, complete and durable responses are seen in only a fraction of cancer patients. A key factor that limits therapeutic success is the lack of T cells in tumor cell regions, a profile termed "immune-excluded." Here, we provide evidence that tumor-associated macrophages (TAMs) are an important determinant of the establishment of a T cell-excluded tumor phenotype. In human and murine tumors, we found that CD8 T cells poorly migrate and invade tumor nests due to long-lasting interactions with TAMs. The depletion of TAMs restores T cell migration and infiltration into tumor islets and improves the efficacy of anti–PD-1 immunotherapy. This study highlights the rationale of combining approaches targeting TAM and immune checkpoint proteins.

Author contributions: E.P., J.L., D.D., and E.D. designed research; E.P., J.L., L.V., V.F., S.B., C.K.-M., N.B., M.G., J.B., H.O., F.R., and E.D. performed research; A.L., M.A., and D.D. contributed new reagents/analytic tools; E.P., J.L., L.V., V.F., S.B., C.K.-M., N.B., J.B., H.O., and E.D. analyzed data; and E.P. and E.D. wrote the paper.

The authors declare no conflict of interest.

This article is a PNAS Direct Submission.

[1]Present address: Translational and Clinical Research, Center for Therapeutic Innovation in Oncology, Servier Research Institute, 78290 Croissy-sur-Seine, France.

[2]To whom correspondence may be addressed. Email: elisa.peranzoni@servier.com or emmanuel.donnadieu@inserm.fr.

This article contains supporting information online at www.pnas.org/lookup/suppl/doi:10.1073/pnas.1720948115/-/DCSupplemental.

Published online April 9, 2018.

of the tissue, and its chemical content, which includes chemokines and antigen doses. These elements vary greatly within tissues and contexts, leading to different T cell motile behaviors.

Tumors are deregulated tissues with abnormal ECM (9). We have previously reported that the dense extracellular matrix found in the stroma of lung and ovarian human tumors is detrimental to T cell displacement and contact with tumor cells (10, 11). In pancreatic tumors, CXCL12 produced by carcinoma-associated fibroblasts has been shown to be another element sequestering CD8 T cells in the tumor stroma, away from tumor cells (12). Growing tumors are enriched in myeloid cells, including macrophages that are susceptible to regulate the scanning process of T cells. In a mouse spontaneous breast tumor model, it has been found that tumor-associated macrophages (TAMs) and CD11b+ dendritic cells (DCs) outnumbered CD103+ DCs, considered to be the most efficient T cell stimulatory antigen-presenting cell (APC) in tumors (13, 14). According to this model, by engaging noneffective APCs, CD8 T cells would be prevented from contacting immunostimulatory CD103+ DCs. It is not known if the same process also occurs in human tumors. In addition, the functional consequences of this CD8 T cell–TAM interaction on tumor growth remain ill-defined.

Here, we investigated the role of TAMs in the control of CD8 T cell distribution and migration in murine and human carcinomas. By using dynamic imaging microscopy, we found that endogenous CD8 T cells form long-lived interaction with TAMs in the tumor stroma. In mouse tumor models, we used PLX3397 (Pexidartinib), a clinically tested inhibitor of CSF-1R, c-kit and Flt3 tyrosine kinases as well as the specific CSF-1R inhibitor PLX5622 to deplete TAMs (15, 16). This treatment markedly increases the number of tumor-infiltrating CD8 T cells, their migration, and their ability to contact tumor cells. This macrophage depletion strategy improves anti–PD-1 cancer immunotherapy, highlighting the importance of the therapeutic modulation of macrophages as an adjuvant therapy for checkpoint inhibitors.

Results

CD8 T Cell Infiltration into Tumor Islets Is a Good Prognostic Parameter in Lung Squamous Cell Carcinoma and Is Related to Lymphocyte Motility. In a cohort of lung squamous-cell carcinoma patients we have analyzed paraffin-embedded tissue sections to obtain insight into the localization of CD8 T cells relative to tumor islets (stained by cytokeratin) and the surrounding stroma. We have noted that, in tumors enriched in CD8 T cells (cutoff of 361 CD8 cells/mm^2), the CD8 tumor-to-stroma ratio (T:S), which reflects the ability of CD8 cells to infiltrate tumor nests, was an independent parameter to discriminate the overall survival of patients, showing that patients with a high T:S ratio (0.16–0.83) had significantly better survival than patients with a ratio lower than 0.15 (Fig. 1*A*, $P = 0.01$). The patients with the best prognosis were those with a high number of CD8 T cells and a high T:S ratio, as a low number of CD8 lymphocytes is associated with reduced overall survival, irrespective of the T:S ratio ("CD8-poor" patients in Fig. S1, $P = 0.7$).

These results prompted us to further analyze the distribution and the real-time motility of endogenous CD8 T cells in the 3D environment of fresh lung squamous-cell carcinomas by a technique using vibratome thick slices that we have recently described (10). In the *Left* panel of Fig. 1*B*, the trajectories and localization of tumor-infiltrating CD8 T cells tracked by real-time microscopy of two representative patients are shown. By means of this approach we were able to observe that, for each microscopic field, the CD8 T cell motility, measured by the displacement length and average speed of the cells, was directly related to the fraction of these cells that infiltrates tumor nests (Fig. 1*B*, *Right*).

We have already observed that in human lung tumors CD8 T cells are enriched in the stroma relative to tumor nests and that this localization is in part dictated by the density and organization of the ECM fibers that can alter lymphocyte motility in the stroma (10, 11). Moreover, lymphocytes migrate more slowly, making reduced displacements in the stroma compared with tumor islets (10). This difference is particularly evident in lung squamous-cell tumors (Fig. 1*C*), and it led us to investigate whether other characteristics of the stromal compartment could impact T cell motility and explain the T cell exclusion profile observed in many cancer patients.

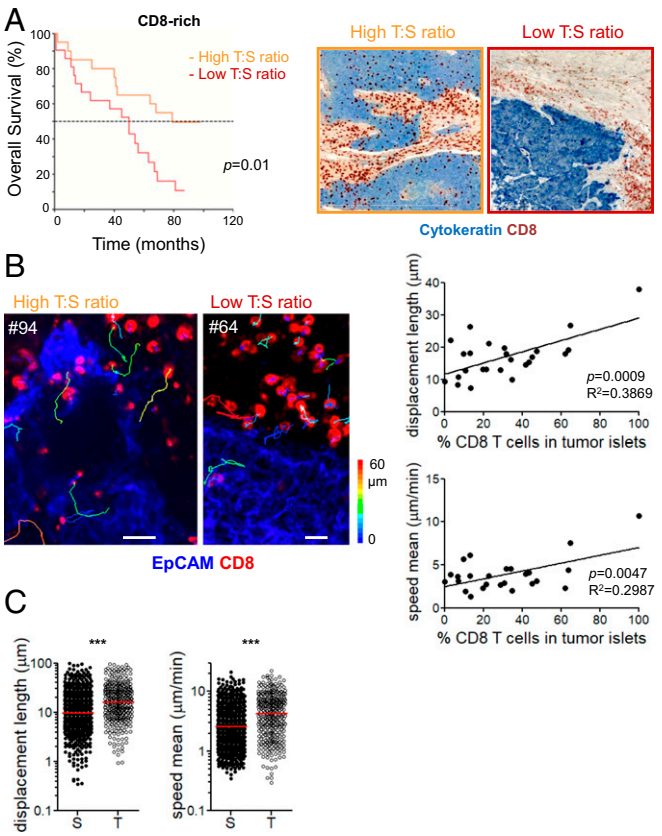

Fig. 1. CD8 T cell infiltration into tumor islets confers a good prognostic value in lung squamous-cell carcinoma and is related to lymphocyte motility. (*A*) Survival analysis of patients with stage I–II squamous-cell carcinomas, according to the density of CD8 T cells in tumor islets. Patients ($n = 51$) with tumor enriched in CD8 T cells were divided into two groups on the basis of the T:S of CD8 T cells. A CD8 T:S value of 0.16 (median) was used as the cutoff to determine high and low groups. Kaplan–Meier curves were used to estimate overall survival of the two groups, and the log-rank test was used to compare the difference between the two curves. (*Right*) Representative images of human lung tumors stained for cytokeratin (blue) and CD8 T cells (red) with a high and a low CD8 T:S ratio. (*B* and *C*) Migration of endogenous CD8 T cells in vibratome sections of viable human lung tumors. (*B*, *Left*) Snapshots of a time lapse with trajectories of individual endogenous CD8 T cells (red) in slices stained with anti-EpCAM (blue) for tumor cells. Tracks are color-coded according to CD8 T cell displacement length. (Scale bars: 20 µm.) Tumor #94 has a high CD8 T:S ratio (0.89), whereas tumor #64 has a low CD8 T:S ratio (0.11). (*B*, *Right*) Displacement length (*Top*) and average speed (*Bottom*) of endogenous CD8 T cells as a function of the percentage of CD8 T cells in tumor islets; $n = 9$. (*C*) Displacement length (*Left*) and average speed (*Right*) of resident CD8 T cells in the stromal and tumor cell regions of human squamous-cell non-small cell lung cancer tumor slices; $n = 9$; medians are shown in red. Mann–Whitney test: ***$P < 0.001$.

CD8 T Cells Are Engaged in Long-Lasting Contacts with Stromal Macrophages That Reduce Their Motility in the Tumor Microenvironment. We explored by immunofluorescence the distribution of the main immune cell populations in the tumor biopsies of patients with lung squamous-cell carcinomas and noted that, similarly to T

lymphocytes, macrophages are also enriched in the stroma compared with tumor nests (Fig. 2*A* and Fig. S2*A*). Macrophages, which can be stained by the CD68 and CD11c markers in these tumors, are often highly enriched in the 25-μm-thick stromal border lining EpCAM$^+$ tumor islets (Fig. S2*B*). Of note, most macrophages in the stroma express the CD206 and CD163 markers, while those that can be found inside the tumor nests in some of the samples rarely express these markers (Fig. S2*C*). As can be observed in Fig. 2*B*, macrophages and CD8 T cells are more often found in contact in the stroma than in the surrounding tumor cell areas. Interestingly, contacts between CD8 T cells and neutrophils are much rarer and are not enriched in the stromal compartment compared with tumor islets (Fig. 2*A* and Fig. S2*D*).

With the aim to understand whether these interactions were able to affect T cell motility in the stroma, we tracked the trajectories of CD8 T cells in squamous-cell fresh tumor slices by fluorescent-coupled Fab antibodies and simultaneously imaged tumor cells (EpCAM$^+$) and macrophages (CD11c$^+$, CD206$^+$, or double-positive). As can be observed in Movies S1 and S2 and in Fig. 2*C*, macrophages form a relatively static cell network while CD8 T cells have a diverse behavior, with some cells migrating actively and others being much less motile. A close examination indicated that arrested CD8 T cells were in contact with TAMs. Moreover, most CD8-TAM contacts in the stroma were long-lasting (at least the duration of the 20-min recording), and, even for shorter interactions, CD8 T cells slowed down in their movements. Indeed, when we measured CD8 T cell displacement length and average speed, we noted that lymphocytes that are in touch with a macrophage at any time during the time lapse showed a reduced motility compared with CD8 T cells that never encountered a macrophage, as revealed by both parameters (Fig. 2*D*). This is further confirmed by the inverse relation that can be observed in these samples between the percentage of stromal CD8 T cells found in contact with a macrophage and the average speed of these lymphocytes in the stroma (Fig. 2*E*).

We have thus hypothesized that, together with other stromal elements such as the ECM fibers and fibroblasts, TAMs can reduce the motility of CD8 T cells in the stroma, contributing to their confinement in this compartment and limiting their entry into tumor nests.

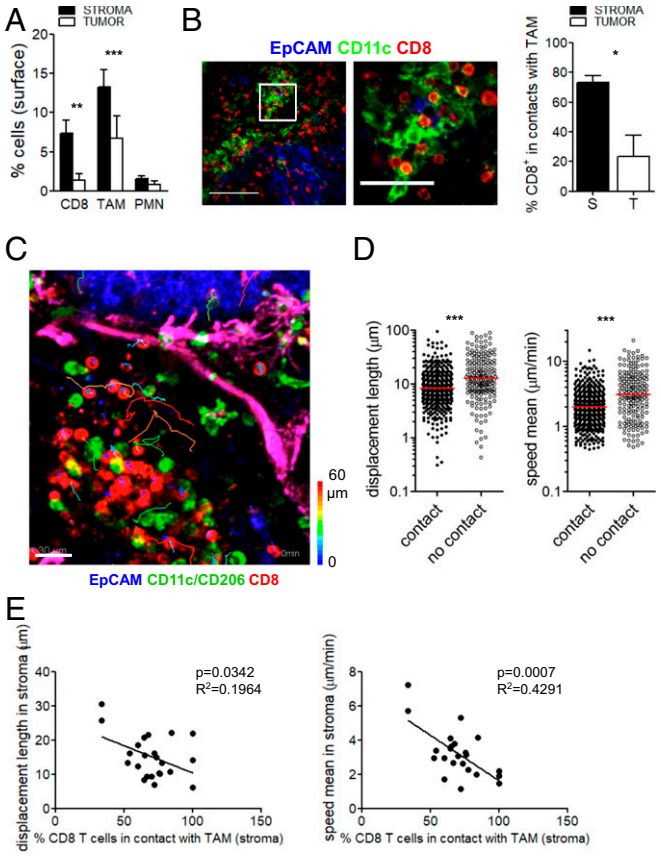

Fig. 2. CD8 T cells are engaged in long-lasting interactions with stromal TAMs in human lung tumors. (*A*–*E*) Localization and migration of endogenous CD8 T cells in vibratome sections of viable human lung tumors. (*A*) Distribution of CD8 T cells, TAMs, and polymorphonuclear cells (PMNs) in the stroma and tumor islets represented as mean ± SEM; $n = 8$. Mann–Whitney test: $^{**}P < 0.01$ and $^{***}P < 0.001$. (*B*, *Left*) Confocal image of a human lung-tumor slice stained for EpCAM (blue), CD11c (green), and CD8 (red). The boxed area is highlighted at higher magnification on the right side. (Scale bars: 100 μm.) (*B*, *Right*) Frequency of CD8 T cells in contact with TAMs; $n = 7$. Mann–Whitney test: $^{*}P < 0.05$. (*C*) Tracks of individual endogenous CD8 T cells in relation to TAMs and EpCAM tumor cells. Tracks are color-coded according to CD8 T cell displacement length. (Scale bar: 30 μm.) See also Movies S1 and S2. (*D*) Displacement length (*Left*) and average speed (*Right*) of endogenous CD8 T cells in contact or not with TAM during a 20-min recording; $n = 9$; Mann–Whitney test: $^{***}P < 0.001$. (*E*) Displacement length (*Left*) and average speed (*Right*) of endogenous CD8 T cells in the stroma as a function of the percentage of CD8 T cells in contact with TAMs in the same region for each microscopic field; $n = 9$ patients, two to four videos for each patient. Each value is the average value for all stromal CD8 T cells of the same slice.

Macrophage Depletion by PLX3397 in Tumor-Bearing Mice Is Able to Increase CD8 T Cell Number and Motility, Leading to Increased Infiltration into Tumor Nests. To verify the impact of macrophages on T cell motility, we performed experiments in two murine models where the depletion of these cells can be easily achieved. We have used both an orthotopic model with transplantation of spontaneous MMTV-PyMT tumors in the mammary fat pad and the s.c. implantation of the Met-1 cell line, derived from spontaneous MMTV-PyMT tumors, in FVB (inbred mouse strain that is named after its susceptibility to Friend leukemia virus B) recipient mice (17). Both tumor models are convenient relative to the spontaneous MMTV-PyMT system, due to their reproducibility and velocity of growth; moreover, in contrast to most cell lines, which exhibit an epithelial-to-mesenchymal transition, they are also very useful for the study of the 3D localization of immune cells, given their resemblance to human carcinomas organized in tumor nests and surrounding stroma (Fig. S3*A*). The depletion of macrophages has been accomplished by means of a CSF-1R, Flt3, and c-kit inhibitor, PLX3397, delivered to mice through the chow 1 wk after tumor implantation until their sacrifice.

In both models, the depletion of macrophages provoked a strong increase in the percentage of CD8 T cells, but not of natural killer (NK) or other myeloid cells, at the tumor site; CD4 T cell number was augmented in the orthotopic PyMT model, but not in Met-1 tumors (Fig. 3*A* and Fig. S3*B*). Despite these changes, PLX3397 administration resulted in a significant reduction in the tumor burden at the moment of sacrifice only in the Met-1 model (Fig. 3*B* and Fig. S3*C*).

When we analyzed lymphocyte motility in fresh tumor slices, we noted that CD8 T cells from PLX3397-treated mice displayed increased average speed and longer displacement lengths compared with mice that were fed with control chow (Fig. 3*C*, Fig. S3*D*, and Movies S3–S8). As PLX3397 inhibits CSF-1R, Flt3, and c-kit, we set out to determine if inhibition of CSF-1R alone was sufficient to exert similar effects on immune cells in tumors. For this purpose, we used PLX5622 that specifically inhibits CSF-1R tyrosine kinase activity with 50-fold selectivity over four related kinases (15). Our results clearly show that inhibition of CSF-1R alone is sufficient to eliminate macrophages and at the same time to increase CD8 T cell number and migratory behavior as shown in Fig. S4. Interestingly, when we considered

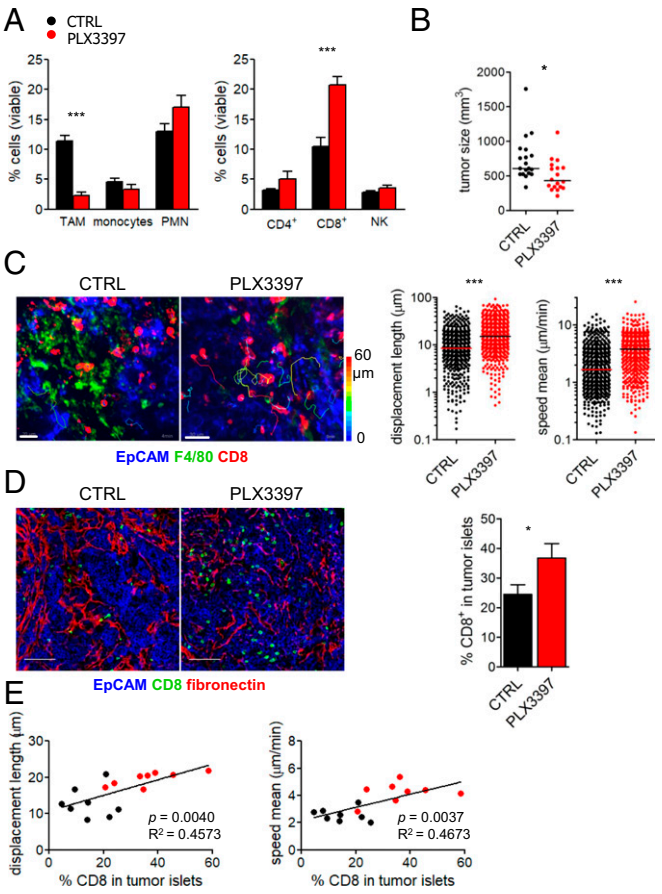

Fig. 3. TAM depletion increases CD8 T cell number, motility, and infiltration into tumor islets of Met-1–bearing mice. FVB mice bearing Met-1 tumors were treated with PLX3397 from day 7. Between day 24 and 28 tumors were resected and analyzed by flow cytometry (*A*) or confocal microscopy (*C*–*E*). (*A*) Frequencies of myeloid subsets (*Left*) and lymphoid subsets (*Right*) among total live cells in tumors. Results are shown as mean ± SEM; n = 16 mice/group from three independent experiments; Mann–Whitney test: ***$P < 0.001$. Macrophages are defined as $CD11b^+Ly6G^-Ly6C^-F4/80^+$, monocytes as $CD11b^+Ly6G^-Ly6C^+$, and polymorphonuclear cell (PMN) as $CD11b^+Ly6G^+Ly6C^{int}$. (*B*) Tumor volumes determined at the sacrifice of mice, n = 22 mice/group. Medians are shown. Mann–Whitney test: *$P < 0.05$. (*C*) Motility of resident CD8 T cells in Met-1 tumor slices from mice treated or not with PLX3397. (*C*, *Left*) Trajectories of individual resident CD8 T cells (red) in relation to $F4/80^+$ TAMs (green) and $EpCAM^+$ tumor cells (blue). (Scale bars: 25 µm.) Tracks are color-coded according to CD8 T cell displacement length. See also Movies S3 and S4. (*C*, *Right*) Displacement length (*Left*) and average speed (*Right*) of endogenous CD8 T cells in tumor slices from mice treated or not with PLX3397; n = 12 mice/group, two to four time lapses/mouse, three independent experiments; Mann–Whitney test: ***$P < 0.001$. (*D*) Distribution of resident CD8 T cells in tumor slices of mice treated or not with PLX3397. (*D*, *Left*) Confocal images. (Scale bars: 100 µm.) (*D*, *Right*) Proportion of CD8 T cells in tumor islets represented as mean ± SEM; n = 11; Mann–Whitney test: *$P < 0.05$. (*E*) Displacement length (*Left*) and average speed (*Right*) of endogenous CD8 T cells as a function of the percentage of CD8 T cells in tumor islets. Black and red points correspond to the control and to the PLX3397 conditions, respectively.

CD8 T cells that can freely migrate (displaying displacement lengths longer than 20 µm in a 20-min recording) we noted that they can achieve identical maximal speed under both control and PLX3397-treated conditions (Fig. S5*A*). This suggests that the soluble microenvironment does not play a major role in inhibiting CD8 T cell migration and that the physical interaction between the two cell types is probably more critical. We then wondered whether the increase in motility provoked by PLX3397 treatment could result in less confinement in the stroma, and thus a better infiltration into tumor islets, of CD8 T cells. Indeed, this was the case in both the Met-1 (Fig. 3*D*) and the orthotopic model (Fig. S5*C*). Moreover, we observed that both parameters of motility that we have considered—the displacement length and the average speed—were directly related to the percentage of CD8 T cells infiltrating tumor nests (Fig. 3*E* and Fig. S5*C*). These results confirm our initial observation made in human samples that macrophages, in addition to their known suppressive properties in growing tumors, might also limit the efficacy of the antitumor response by confining CD8 T cells in the stroma and limiting their contact with tumor cells.

Macrophage Depletion by PLX3397 in Tumor-Bearing Mice Does Not Affect the Structure of the Extracellular Matrix. Our previous study conducted on human lung and ovarian tumors demonstrated that the structure of the ECM controls T cell migration within tumors and their ability to contact malignant cells, with loose fibronectin and collagen regions promoting T cell migration and dense matrix areas having the opposite effects (10, 11). Thus, one possible mechanism by which T cells migrate more actively in the absence of macrophages could be a decrease in the ECM. To test the impact of macrophage depletion on the structure of the ECM, we performed immunostaining experiments to assess fibronectin distribution in Met-1 tumors from mice treated or not with PLX3397 (Fig. S6). In Met-1 tumors, stromal regions enriched in fibronectin account for 30% of the total surface of slices, and no differences were observed between control and PLX3397 conditions (Fig. S6*B*). We then analyzed the density of fibronectin fibers in the stroma in both conditions, and again we did not evidence any difference (Fig. S6*C*). Thus, depletion of TAMs with PLX3397 does not change the structure of the ECM in these tumor models. These results suggest that the increase in CD8 T cell number and migration observed after PLX3397 treatment is not due to loosening of the ECM.

The Combination of PLX3397 with the Checkpoint Inhibitor Anti–PD-1 Further Increases CD8 T Cell Recruitment at the Tumor Site and Reduces Tumor Burden. Even though the depletion of macrophages was followed by an increase in CD8 T cell number at the tumor site and a better infiltration of lymphocytes inside tumor nests, this was not accompanied by major effects on tumor growth. However, we noted that intratumoral CD8 T cells show high expression of PD-1 and that this expression is further increased following the administration of PLX3397 (Fig. S7*A*). Moreover, an increase in the release of IFN-γ, GM-CSF, and CCL2 in the supernatant of whole-tumor slices was observed in PLX3397-treated tumors, suggesting that the strong reduction in the number of macrophages can modify the tumor microenvironment, facilitating CD8 T cell recruitment (maybe through a reduced competition for the chemokine CCL2, used by monocytes and T cells) and supporting a less suppressive environment (Fig. S7*B*).

The effect of PLX3397 on T cell migration and localization, as well as the phenotype of CD8 tumor-infiltrating lymphocytes (TILs), prompted us to combine this depletion strategy with an anti–PD-1, an immune checkpoint inhibitor that is increasingly being used in the therapy of solid tumors, including lung carcinomas. FVB transplanted mice were treated with PLX3397 or control chow from 7 d after tumor injection up to their sacrifice and received i.p. injection of anti–PD-1 or isotype control antibody every 4 d after PLX3397 treatment. While the anti–PD-1 antibody alone was able to reduce tumor growth in the orthotopic, but not the Met-1, model, the combination of PLX3397 with the checkpoint inhibitor had a strong effect in both systems (Fig. 4*A* and Figs. S8 and S9*A*). When we analyzed the cellular infiltrate of these tumors, we could observe that the anti–PD-1 alone did not have any effect on the immune composition

of the microenvironment (Fig. 4*B* and Fig. S9*B*). On the contrary, the combination therapy further expanded the percentage of CD8 T cells compared with PLX3397 alone in the PyMT model; in addition, it also increased the percentages of CD4 T cells and, at least in the Met-1 model, of NK cells (Fig. 4*B* and Fig. S9*B*, *Right*). In all of the performed experiments, the number of CD8 T cells was inversely related to tumor size, highlighting the importance of this parameter in tumor growth control and in the response to anti–PD-1 therapy (Fig. 4*C* and Fig. S9*C*).

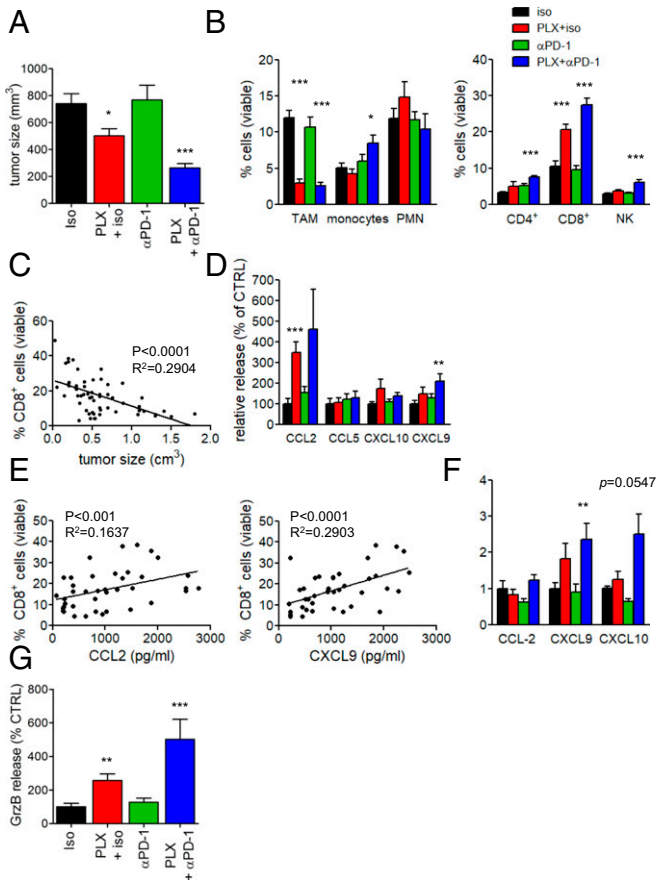

Fig. 4. TAM depletion enhances anti–PD-1 immunotherapy in tumor-bearing mice. FVB mice bearing MET-1 tumors were treated with PLX3397 from day 7. On days 9, 12, 15, and 18, mice were treated or not with anti–PD-1 or control IgG by i.p. injection. Tumors were collected and analyzed between days 24 and 28. (*A*) Tumor volume for each treatment group. Results are shown as mean ± SEM; $n = 21$ mice/group from three independent experiments. Mann–Whitney test, isotype vs. other groups: $^{*}P < 0.05$ and $^{***}P < 0.001$. (*B*) Frequencies of myeloid subsets (*Left*) and lymphoid subsets (*Right*) among total live cells in tumors determined by flow cytometry. Results are shown as mean ± SEM; $n = 15$ mice/group from three independent experiments; Mann–Whitney test, isotype vs. other groups: $^{*}P < 0.05$ and $^{***}P < 0.001$. (*C*) Proportion of CD8 T cells among total live cells as a function of tumor volumes determined at the endpoint; $n = 60$. (*D*) Luminex analysis of inflammatory chemokines produced by fresh Met-1 tumor slices kept in culture for 18 h; $n = 10$ mice/group from three independent experiments. Mann–Whitney test, isotype vs. other groups: $^{**}P < 0.01$ and $^{***}P < 0.001$. (*E*) Proportion of intratumoral CD8 T cells among total live cells as a function of CCL2 (*Left*) and CXCL9 (*Right*) produced by Met-1 tumor slices kept in culture for 18 h. (*F*) Chemokine mRNA levels of Met-1 cells sorted from fresh tumors. The expression levels of chemokines were analyzed by qRT–PCR; $n = 6$ mice/group from two independent experiments; Mann–Whitney test, isotype vs. other groups: $^{**}P < 0.01$. (*G*) Granzyme B release in the supernatant of fresh Met-1 tumor slices kept in culture for 18 h were measured by ELISA; $n = 10$ mice/group from three independent experiments; Mann–Whitney test, isotype vs. other groups: $^{**}P < 0.01$ and $^{***}P < 0.001$.

When we analyzed the supernatants of the tumor slices derived from these experiments, we noted that the combination therapy led to a milieu of chemokines that could further support T cell infiltration compared with either approach alone (Fig. 4*D* and Fig. S9*D*). Indeed, CCL2 and CXCL9 are directly related to the percentage of CD8 T cells present at the tumor site, indicating that these chemokines are critical in recruitment of effector cells (Fig. 4*E*), while CCL5 does not seem to be involved in these tumor models (Fig. 4*D*). Moreover, CXCL9 and CXCL10, the main ligands of CXCR3, are up-regulated in isolated tumor cells following the combination of PLX3397 and anti-PD1 (Fig. 4*F*), suggesting that this treatment could induce the expression of chemokines promoting the infiltration of lymphocytes into tumor islets. Consistent with the observed increase of effector cells at the tumor site and the reduction in tumor size, granzyme B secretion in tumor slices was strongly augmented with the combination therapy (Fig. 4*G*).

The Combination of PLX3397 and Anti–PD-1 Results in the Presence of Numerous CD8 T Cells Engaged in Stable Contact with Tumor Cells. We then analyzed by confocal microscopy the localization and motility of CD8 T cells on tumor slices following these treatments. The administration of the anti–PD-1 alone did not change the concentration and the tumor:stroma distribution of CD8 T cells, indicating that the PD-1/PD-L1 interaction is probably not critical in the retention of lymphocytes mediated by macrophages (Fig. 5*A* and Fig. S9*E*). By comparison, the combination therapy markedly increased the proportion of CD8 T cells in tumor islets, even more than under the PLX3397 condition (Fig. 5*A* and Fig. S9*E*). The analysis of CD8 T cell motility in tumor islets confirmed that resident CD8 T cells in tumors from mice treated with PLX3397 migrate actively as attested by their displacement lengths and average speed (Fig. 5*B*). Interestingly, the combination therapy resulted in a low motility of CD8 T cells, suggesting that the anti–PD-1 could modify the duration of the contacts between cytotoxic lymphocytes and tumor cells when macrophages were not present (Fig. 5*B*). Hence, the frequency of arrested CD8 T cells in tumor islets, defined as cells that have an average velocity of less than 2 μm/min during a 20-min recording, was increased in the combination treatment compared with the PLX3397 condition (Fig. S10). When we combined the fraction of CD8 T cell infiltrating the tumor nests and the fraction of arrested lymphocytes in this compartment, we found that PLX3397+anti–PD-1 treatment resulted in an increased proportion of low motile CD8 T cells in tumor islets compared with the other conditions (Fig. 5*C*).

Overall, the release of CD8 T cells from the stroma achieved through macrophage depletion allows for better lymphocyte infiltration into tumor nests and scanning of tumor cells. Under these conditions, PD-1 blockade promotes T cells to decelerate, likely forming productive contact with tumor cells leading to their destruction.

Discussion

Growing evidence supports the notion that clinical response to anti–PD-1 immunotherapies is associated with the presence of CD8+ T cells in tumor cell regions before the treatment (5). Strikingly, the accumulation of CD8+ T cells in the stroma that surrounds nests of tumor cells is not sufficient, as cancer patients harboring this tumor phenotype do not respond to anti–PD-1 antibodies (5). There is therefore a considerable interest in elucidating the molecular and cellular mechanisms underlying T cell exclusion from tumor islets (2, 6). Our current work provides evidence that TAMs are a key determinant of the establishment of a T cell-excluded tumor phenotype. Our data indicate that, in human and murine tumors, CD8 T cells migrate poorly and invade tumor nests due to long-lasting interaction with tumor-associated macrophages in the stroma. The depletion

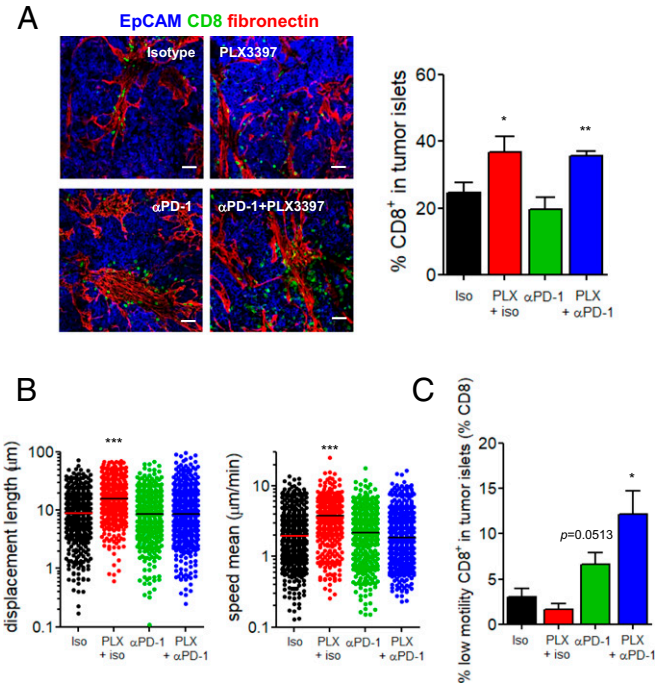

Fig. 5. Combination therapy of CSF-1R inhibitor and anti–PD-1 affects CD8 T cell number and motility in tumor islets. FVB mice bearing MET-1 tumors were treated with PLX3397 from day 7. On days 9, 12, 15, and 18, mice were treated or not with anti–PD-1 or control IgG. Tumors were collected and analyzed by confocal microscopy from days 24–28. (*A*) Distribution of resident CD8 T cells in Met-1 tumors for each condition. (*A*, *Left*) Confocal images of Met-1 tumor slices stained for EpCAM (blue), CD8 T cells (green), and fibronectin (red). (Scale bars: 100 μm.) (*A*, *Right*) Fraction of resident CD8 T cells in tumor islets of Met-1 tumors; $n = 10$ mice/group from three independent experiments; Mann–Whitney test, isotype vs. other groups: $*P < 0.05$ and $**P < 0.01$. (*B*) Displacement length (*Left*) and average speed (*Right*) of endogenous CD8 T cells in the stroma and tumor islets of Met-1 tumor slices; $n = 7$ mice/group from three independent experiments, two to three time lapses/mouse. Mann–Whitney test, isotype vs. other groups: $***P < 0.001$. (*C*) Fraction of total CD8 T cells residing in tumor islets and displaying low motility (average speed: <2 μm/min); $n = 7$ mice/group from three independent experiments, two to three time lapses/mouse; Mann–Whitney test: $*P < 0.05$.

of TAMs restored CD8 T cell migration and infiltration into tumor islets and improved the efficacy of anti–PD-1 immunotherapies.

Various macrophage phenotypes are present within the tumor microenvironment. In progressing tumors, the dominant phenotype is reported to be antiinflammatory, immune regulatory as opposed to proinflammatory and tumoricidal (18, 19). Thus, various strategies have been developed to target TAMs (20). Macrophages depend on the CSF-1 signaling axis for their recruitment and survival into tissues. In this study, we used PLX3397 (pexidartinib), a clinically tested inhibitor of CSF-1 receptor, Flt3, and c-kit, but also PLX5622, a more specific CSF-1R inhibitor, to deplete TAMs and assess its consequence on resident CD8 T cells (15, 16). Using two different mouse tumor models, our data indicate that CSF-1R inhibition resulted in an increased number of CD8 T cells within the tumor, a result consistent with previous studies (21, 22). Notably, other myeloid populations including monocytes and neutrophils were not depleted by CSF-1R blockade, ruling out an effect of these cells on T cell number and motility observed here. Targeting CCR2, a chemokine receptor expressed by several myeloid cells, has also been shown to increase the frequency of T cells within murine tumors (23). However, we extended these results to show, using dynamic imaging microscopy on fresh tumor slices, that CSF-1R blockade increased resident CD8 T cell motility and, importantly, CD8 T cell capacity to infiltrate tumor islets.

Two-photon imaging experiments performed in mouse models have led to the conclusion that T cells are endowed with a scanning activity regulated by a variety of environmental factors (7). Positive regulators of T cell motility include chemokines and a loose fiber network such as those observed in lymphoid organs, whereas a dense environment and potent antigen recognition decrease T cell motility. In progressing tumors, our previous study and this current one provide the evidence that T cells in the stroma are impaired in their motility and thus unable to infiltrate tumor islets. Over the years, different stromal obstacles have been identified, including a dense ECM and a high concentration of CXCL12 (6). Our data add TAMs to the list of elements having detrimental effects on T cell migration within the tumor stroma.

Several mechanisms can be envisioned for the recovery of CD8 T cell scanning behavior after macrophage depletion. A change in the adhesive environment that CD8 T cells encounter in the tumor stroma might explain the increased T cell scanning activity and infiltration into tumor islets following CSF-1R inhibition. Macrophages are antigen-presenting cells that express numerous adhesion molecules for T cells. In inflammatory settings such as granuloma and multiple sclerosis, macrophages have been shown to form conjugates with T cells, retaining them in discrete areas (24, 25). In two mouse-tumor models expressing ovalbumin, a meshwork of myeloid cells composed of TAMs and $CD11b^+$ DCs was reported to form long-lasting interactions with OVA-specific CD8 T cells (14, 26). Further research is warranted to determine whether the conjugates formed between TAMs and CD8 T cells in the stroma are dependent on antigen recognition. However, this TAM retention mechanism might be a more general process affecting other subtypes of T cells, such as CD4 T cells in tumors and γδT cells in lymph nodes (27).

A change in the tumor microenvironment promoting T cell migration also cannot be ruled out. Following CSF-1R inhibition, we evidenced more CCL2 and a tendency for more CXCL9 and CXCL10, an effect increased by the combination with a PD-1 blockade, in line with previous studies (22). We also found that these chemokines were directly related to the amount of TILs in the tumor, confirming their importance in recruiting CD8 T cells. Evidence suggests a requirement for the CXCR3-CXCL9/CXCL10 axis for CD8 T cell trafficking to tumors (28). The nature of the cells producing CCL2, CXCL9, and -10 and the number and/or function of which is affected upon CSF-1R inhibition remains to be established. Tumor cells, as well as CD103 DC, recently shown to attract T cells into tumors through the production of CXCR3 ligands, are good candidates (29). The mechanism by which the depletion of TAMs increases the amount of inflammatory chemokines in tumors is not known at present. The recent report of a role of galectin-3, produced by tumor cells but also TAMs, in the reduction of CXCL9 and CXCL10 could provide an interesting explanation of the effects reported here (30).

In a number of tissues including tumors, TAMs have been demonstrated to support the formation of a dense extracellular matrix (31). Knowing the detrimental effect of tumor fibrosis on the capacity of T cells to infiltrate tumor islets (10, 11, 32), we initially thought that TAM depletion would have led to a reduction in ECM fiber deposition. However, our data do not support such an hypothesis, as the distribution of fibronectin fibers is similar in the presence or absence of macrophages.

In line with previous studies (21, 22, 33, 34), we found that CSF-1R inhibition alone has a minor influence on tumor growth, suggesting that an increase in T cells and their motility is not sufficient to promote tumor regression. The augmentation in some cytokines and chemokines in granzyme B and in the expression of PD-1 by CD8 T lymphocytes likely implies that TAM depletion induces a partial activation of T cells that may lead to

exhaustion, in part due to the engagement of PD-1 with its ligand and thus to an incomplete antitumor response. However, our data indicate that CSF-1R inhibition combined with anti–PD-1 therapy markedly decreases tumor growth. Interestingly, in other tumor models, CSF-1R inhibitors have been shown to improve chemo- and radiotherapy, cellular therapies such as adoptive T cell transfer, and immune checkpoint inhibitor immunotherapies (21, 22, 33, 34).

Together with an effect on tumor growth, we showed that the combination of PLX3397 with PD-1 blockade further increased the density of CD8 T cells in tumor islets and promoted their arrest in this region compared with the anti-CSF1R condition alone. This combined treatment is also associated with a higher total release of Granzyme B compared with other conditions.

A deceleration of CD8 T cells in tumor islets observed in the combination therapy is consistent with two-photon imaging studies showing that effective immunotherapy treatment resulted in T cell arrest on tumor cells during the early phase of tumor regression, compatible with an effective antigen recognition and tumor cell killing (35–38). Of note, the motile behavior of T cells at later time points during tumor regression seems different, and several studies suggest that T lymphocytes resume their migration, allowing them to progress toward the center of the tumor (35, 39). Our data extend these findings by distinguishing the behavior of resident CD8 T cells in the stroma and tumor islets, something that has rarely been done due to the use of mouse tumor models usually devoid of a structural organization.

How does PD-1 blockade decrease T motility in tumor islets in the absence of TAMs? These past few years, the role of PD-1 in controlling T cell displacement and conjugate formation with antigen-presenting cells has been investigated in different contexts (40–43). During acute immune responses, the expression of PD-1 at the surface of activated T cells inhibits the formation of a stable antigen-dependent contact with the antigen-presenting cells (40, 41). In such settings, PD-1 blockade promoted T cell arrest. Our data are in line with this notion and show that when CD8 T cells are allowed to infiltrate and migrate within tumor islets—in the anti-CSF1R condition—PD-1 blockade promotes T cell deceleration and arrest. Although this point will need further investigation, the numerous arrested TILs in tumor islets are likely responsible for the killing of tumor cells. In addition, the increased number of activated TILs observed after the dual treatment likely creates an inflammatory milieu with the production of more chemokines favoring the recruitment of additional T cells. Taken together, our data support the notion that anti–PD-1 antibodies are effective only in the presence of numerous T cells in tumor islets, consistent with clinical data (5).

It is clearly established that a subset of TAMs suppresses the TIL antitumor responses and is associated with a bad outcome in cancer patients. Many mechanisms have been proposed, such as a block of T cell proliferation or their cytotoxic activities (18, 19). Here, we uncover a mechanism by which TAMs suppress T cell antitumor activities through inhibiting their tumor surveillance scanning activity and therefore contact with malignant cells. Together with carcinoma-associated fibroblasts producing dense ECM and CXCL12, TAMs might create an immunosuppressive environment leading to the establishment of a T cell-excluded profile observed in a variety of solid tumors. This notion is in line with recent clinical and genomic studies. By analyzing molecular signatures of pretreatment tumor specimens, Hugo et al. (44) found a pattern of genes associated with resistance to PD-1 therapy. Genes involved in mesenchymal transition, extracellular matrix remodeling, angiogenesis, wound healing, and macrophage infiltration were enriched in nonresponding tumors. Of note, M2-like CD206 macrophages are known to play important roles in promoting each of these processes (45). In human colorectal tumors, a similar mesenchymal signature, associated with a bad outcome, is characterized by a proinflammatory, proangiogenic, and immunosuppressive microenvironment with high lymphocyte and myeloid cell infiltration (46, 47). Unrelated to the latter mechanisms, it has recently been suggested that TAMs promoted resistance to anti–PD-1 strategy through another mechanism dependent on Fc receptors and the removal of the monoclonal antibody from T cells (48).

Even though the mechanism and the molecules involved in macrophage-dependent T cell retention still remain to be uncovered, we hypothesize that this phenomenon might be another consequence of the physical interaction between macrophages and lymphocytes observed in tumors. As previously discussed, long-lasting interactions between antigen-specific CD8 T cells and antigen-presenting macrophages have been described in a B6-PyMT model, and they have been associated with T cell inhibition (14). Moreover, in FVB PyMT mice, TAMs have also been shown to mediate suppression of T cells in vitro and in vivo (33). So the close interplay between macrophages and T cells that is known to cause immunosuppression could also lead to lymphocyte retention in the stroma, further inhibiting efficient T cell killing of tumor cells.

In these interactions, we currently do not know what the impact of antigen presentation is, but suppression is likely predominant, as the depletion of macrophages allows for an even better antitumor response compared with nondepleted animals, suggesting that other cell types or residual macrophages still exert the presentation of tumor antigens.

Developing therapeutic strategies that help overcome a lack of T cell unresponsiveness to tumor antigen and a lack of infiltration of T cells into tumor islets is critical to increase the fraction of patients responding to immunotherapy. A scheme would be to transform tumors with a stromal T cell profile into inflamed tumors with numerous T cells in contact with malignant cells that would therefore be responsive to anti–PD-1 treatment. Approaches that target cells such as TAMs or factors including TGFβ, responsible for the formation of a mesenchymal stroma and for immunosuppression, are promising (2). Clinical studies are now ongoing in several solid tumor types where macrophages are targeted by CSF-1R inhibitors (49). However, recent evidence suggests that, in certain contexts, macrophages can cooperate with T cells to promote tumor regression (50, 51). Thus, instead of depleting all macrophages, an alternative strategy would consist of promoting macrophage activation (52) or reprogramming macrophages toward an antitumor phenotypic state (53), which would support T cell migration and function and, together with immune checkpoint blockade therapy, limit ongoing tumor growth.

Materials and Methods

Primary Lung Squamous-Cell Carcinoma Cohort. A retrospective consecutive cohort of 101 patients with lung squamous-cell carcinomas treated by primary surgery between June 2001 and December 2005 at the Department of Thoracic Surgery, Hôtel-Dieu Hospital (Paris) was assessed. Patients with previous lung cancer or other synchronous cancers or induction treatments were excluded. All had lobectomy or pneumonectomy with radical nodal dissection and complete resection (R0). Formalin-Fixed Paraffin-Embedded (FFPE) primary lung-tumor samples were obtained for each patient and used to study by immunohistochemistry the immune composition of the tumor microenvironment. Minimum follow-up was 80 mo for the last patient included in the cohort. The observation time of the cohort was the interval between tumor resection and the last contact (last follow-up or death of the patient).

Immunohistochemistry. For each FFPE lung-tumor sample, two observers, including at least one expert pathologist, selected the tumor section containing the highest density of immune cells on hematoxylin-eosin-safran–stained slides. Paraffin section was dewaxed, followed by antigen retrieval with EDTA (pH 8) in a preheated water bath (97 °C, 30 min). Endogenous peroxidase was blocked for 15 min with 3% hydrogen peroxide followed by an incubation with diluted 5% human serum for 30 min. Thereafter tissue sections were incubated with primary antibodies for 1.5 h at room temperature

(rabbit anti-human CD8, SP16 clone from Springbiosciences, mouse anti-human cytokeratin, AE1/AE3 clone from Dako) and followed by secondary antibodies coupled with biotin or alkaline phosphatase (biotinylated donkey anti-rabbit #711.066.152 and goat anti-mouse IgG-AP #115–056-062 from Jackson ImmunoResearch). Biotinylated antibodies were coupled with streptavidin–peroxidase, and peroxidase activity was revealed using 3-amino-9-ethylcarbazole substrate (Vector Laboratories). Alkaline phosphatase activity was revealed using alkaline phosphatase substrate III (Vector Laboratories).

Slides were scanned by using a Nanozoomer scanner (Hamamatsu) and analyzed with NDPview software. Calopix software (Tribvn) was used to count CD8 T cells in tumor nests and in the tumor stroma. Areas of the whole-tumor section, tumor nests, and tumor stroma were determined by the Calopix software. Results are expressed as the absolute number of positive cells per square millimeter.

Tumor Slice Imaging. Fresh lung tumors were obtained from anonymized patients diagnosed with clinical stage I–II non-small cell lung cancer who had undergone primary lobectomy or pneumonectomy. Nonfixed fresh tumors obtained after resection were rapidly transported to the laboratory in ice-cold RPMI 1640. Tumors with a very high level of autofluorescence of fibers precluding imaging of T cells, with an unclear distinction between tumor-cell regions and stroma or with complete immobility of CD8 T cells in the whole tissue, were discarded after visual inspection of several microscopic fields or time-lapse imaging of immunostained tumor slices. Experiments were performed with tumor specimens obtained 2–4 h after tumor resection. A minority of biopsies was kept 12–24 h at 4 °C before processing for imaging, and similar results were obtained with these samples in terms of T cell motility. Tumor slices were prepared as described in refs. 10 and 11. Briefly, samples were embedded in 5% low-gelling-temperature agarose (type VII-A; Sigma-Aldrich) prepared in PBS. Slices (350 μm) were cut with a vibratome (VT 1000S; Leica) in a bath of ice-cold PBS. Slices were then transferred to 0.4-μm organotypic culture inserts (Millicell; Millipore) in 35-mm petri dishes containing 1.1 mL RPMI 1640 without Phenol Red. Live vibratome sections were stained for 15 min at 37 °C with the following antibodies: BB515 anti-human CD11c (B-ly6 clone; BD Biosciences), PE–anti-human CD206 (19.2 clone; BD Biosciences), AlexaFluor647–anti-human CD8a Fab fragment (clone B-Z31; R&D Biotech) or AlexaFluor647 anti-human CD8a (SK1 clone; BD Biosciences) and BV421–anti-human EpCAM (9C4 clone; BioLegend). All antibodies were diluted in RPMI without Phenol Red and used at a concentration of 10 μg/mL. For distinguishing tumor islets from stroma, second harmonic generation signal or BV510 anti-human Thy-1 (5E10 clone; BD Biosciences) staining were used, depending on the microscope. To concentrate the antibodies on the tissue, a stainless steel ring was placed on the agarose surrounding the slice.

Murine tumors were embedded in agarose and cut into 350-μm-thick viable slices after resection, following the same protocol described for human biopsies. For dynamic imaging, murine slices were stained, following the previously described protocol, with the following antibodies: APC anti-mouse CD8a (REA601; Miltenyi Biotec), AlexaFluor488 anti-mouse F4/80 (A3-1 clone; Bio-Rad), PE anti-podoplanin (8.1.1 clone; BioLegend), and BV412 anti-mouse EpCAM (G8.8 clone; BD Biosciences).

T cells were imaged with a DM500B upright microscope equipped with a SP5 confocal head (Leica) or with an upright spinning disk confocal microscope (Leica), both equipped with a 37 °C thermostated chamber. For dynamic imaging, tumor slices were secured with a stainless steel slice anchor (Warner Instruments) and perfused at a rate of 0.8 mL/min with a solution of RPMI without Phenol Red, bubbled with 95% O_2 and 5% CO_2. Ten minutes later, images from a first microscopic field were acquired with a 25× water immersion objective (20×/0.95 N.A.; Olympus). For four-dimensional analysis of cell migration, stacks of 10–12 sections (z step = 5 μm) were acquired every 30 s for 20 min at depths up to 80 μm. Regions were selected for imaging when tumor parenchyma, stroma, and T cells were simultaneously present in the same microscopic field. For most of the tumors included in the study, between two and four microscopic fields were selected for time-lapse experiments.

Data Analysis. Image analysis was performed at the Cochin Imaging Facility (Institut Cochin, Paris). A 3D image analysis was performed on *x*, *y*, and *z* planes using Imaris 7.4 (Bitplane AG). First, superficial planes from the top of the slice to 15 μm in depth were removed to exclude T cells located near the cut surface. Cellular motility parameters were then calculated using Imaris. Tracks >10% of the total recording time were included in the analysis. When a drift in the *x*, *y* dimension was noted, it was corrected using the "Correct 3D Drift" plug-in in ImageJ.

Immunofluorescence on Fixed Tumor Slices. For most of the tumors, half of the biopsy was fixed overnight at 4 °C in a periodate–lysine–paraformaldehyde solution [0.05 M phosphate buffer containing 0.1 M L-lysine (pH 7.4), 2 mg/mL NaIO4, and 10 mg/mL paraformaldehyde]. Fixed tumors were then embedded in agarose and cut into 350-μm-thick slices as previously described. Human slices were stained for 15 min at 37 °C with the following antibodies: BB515 anti-human CD11c (B-ly6 clone; BD Biosciences), PE–anti-human CD206 (19.2 clone; BD Biosciences), AlexaFluor647–anti-human CD8a (SK1 clone; BD Biosciences), PerCP/Cy5.5 anti-human CD15 (W6D3 clone; BioLegend), BV421–anti-human EpCAM (9C4 clone; BioLegend), and BV510 anti-human Thy-1 (5E10 clone; BD Biosciences). Murine slices were fixed, cut, and stained following the same protocol, with the following antibodies: rabbit anti-mouse/human fibronectin (Sigma), followed by an AlexaFluor488 anti-rabbit IgG (Invitrogen), PerCP-eFluor710 anti-mouse CD8a (53-6.7 clone; eBioscience), PE anti-mouse F4/80 (A3-1 clone; Bio-Rad), eFluor660 anti-podoplanin (8.1.1 clone; eBiosciences), and BV412 anti-mouse EpCAM (G8.8 clone; BD Biosciences). The z-stack images of 5 × 5 fields were taken with a 25× water immersion objective (25×/0.95 N.A.) on an upright spinning disk confocal microscope (Leica). Virtual slices were reconstituted and analyzed with ImageJ software.

Statistical Analysis. Kaplan–Meier curves were used to estimate the overall survival. Group comparison was carried out by the log-rank test. To assess difference in survival according to the CD8 T:S ratio, a value of 0.16 (median) was chosen as the cutoff. The start of follow-up for overall survival was the time of surgery. Patients were followed up to death or to August 2013. All patients alive at this date were censored.

For immunofluorescence and flow cytometry data comparison, an unpaired two-tailed nonparametric Mann–Whitney test was performed to determine statistical significance. All these statistical analyses were performed with Prism 6 (GraphPad). $*P < 0.05$, $**P < 0.01$, and $***P < 0.001$.

Animal Studies. FVB mice were purchased from Charles River and Janvier laboratories. Mice were maintained in the Cochin Institute specific-pathogen–free animal facility. Animal care was performed by expert technicians in compliance with the Federation of European Laboratory Animal Science Associations.

For the MMTV-PyMT transplanted model, tumors from 3-mo-old MMTV-PyMT FVB mice were isolated after sacrifice. Tumors were mechanically disaggregated and incubated for 45 min at 37 °C with freshly made RPMI dissociation buffer including DNase (100 μg/mL; Roche), collagenase (1 mg/mL; Roche), and hyaluronidase (1 μg/mL; Sigma) under gentle agitation. The obtained solution was filtered on a 40-μm cell strainer in 2% FCS 1 mM EDTA PBS. Red blood cell lysis was performed using ammonium–chloride–potassium (ACK) buffer. Finally, cells were washed and resuspended in PBS at the appropriate concentration. Eight-week-old FVB recipient mice were transplanted subcutaneously (day 0) in the right inferior mammary fat pad with 10^6 cells obtained from MMTV-PyMT tumors.

For the Met-1 model, the Met-1 cell line derived from MMTV-PyMT tumors, obtained from Robert Cardiff (University of California, Davis) (17), was maintained in culture in complete RPMI, including 10% FBS (GE Heathcare), 50 U/mL penicillin, 50 μg/mL streptomycin (GIBCO), 4 mM L-glutamine (GIBCO), and 1 mM Hepes (GIBCO). Eight-week-old FVB mice were transplanted s.c. (day 0) in the right flank with 10^6 Met-1 cells.

When tumors reached a diameter of 6 mm (~7–8 d), mice were fed either with chow containing PLX3397 (275 mg/kg), PLX5622 (1,200 mg/kg) or with control chow (Plexxikon) until sacrifice. Four i.p. injections of 200 μg of anti–PD-1 antibody (RMP1-14 clone; BioXcell) or isotype control (rat IgG2a; BioXCell) were performed from day 10 every 4 d. Tumors were measured every 3 d, and the tumor volumes were estimated by tumor volume = width × width × length/2. At sacrifice, tumor volumes were estimated by tumor volume = width × length × height.

Flow Cytometry. Tumors were mechanically dissociated and digested for 45 min at 37 °C in RPMI 1640 with 37.5 μg/mL Liberase TM (Roche) and 8,000 U/mL DNase I, bovine pancreas (Merck Millipore). After red blood cell lysis with ACK buffer and filtration on a 40-μm cell strainer, the cell suspension was rinsed in PBS and stained in 96-well round-bottom plates with a LIVE/DEAD Fixable Blue Dead Cell Stain Kit (Invitrogen) for 20 min at 4 °C. Cells were then washed and stained with antibodies for surface markers for 20 min at 4 °C. The following antibodies were purchased from BD Bioscience: BV711 anti-mouse CD4 (GK1.5 clone), PE/Cy7 anti-mouse CD11b (M1/70 clone), AlexaFluor700 anti-mouse CD45 (30-F11 clone), BV421 anti-mouse EpCAM (G8.8 clone), BV605 anti-mouse TCRβ (H57-597 clone), and FITC anti-mouse Ly6G (1A8 clone). BV786 anti-mouse CD11b (M1/70 clone), BV605 anti-mouse CD11c (N418 clone), BV711 anti-mouse CD206 (CO68C2), BV510

anti-mouse Ly6C (HK1.4 clone), and BV785 anti-mouse MHC II (M5/114.15.2 clone) were purchased from BioLegend. PE anti-F4/80 (A3-1 clone) was purchased from Bio-Rad. PerCP eFluor710 anti-mouse CD8a (53-6.7 clone) and eFluor660 anti-mouse CD335 Nkp46 (29A1.4 clone) were purchased from eBioscience. After surface staining, cells were fixed with BD Fixation and Permeabilization Solution for 20 min at 4 °C. After washing in PBS, cells were resuspended in PBS 2% FBS and analyzed with a BDFortessa flow cytometer (BD Bioscience). Data were analyzed by FlowJO.

For the assessment of chemokine expression by qRT-PCR in tumor cells, $EpCAM^+$ cells were FACS-sorted on a FACSAria instrument (BD Biosciences) after depletion of $CD45^+$ cells with CD45 MicroBeads (Miltenyi Biotec).

Granzyme B, Cytokine, and Chemokine Detection in Tumor Slice Supernatants. Fresh tumor slices were prepared as previously described and kept at 37 °C in 24-well plates with 0.5 mL RPMI per well. Four to five slices were put in culture for each mouse. Eighteen hours later supernatants were collected and centrifuged at 300 × *g* to eliminate suspension cells. Cell-free supernatants were frozen and stored at 80 °C. Granzyme B release in the supernatants was measured by ELISA (Affymetrix Ebioscience). Cytokine and chemokine release was assayed by Luminex technology (Bio-Plex 200 from Bio-Rad) with a customized Milliplex kit (Merck Millipore).

RNA Extraction and Real-Time qRT-PCR. Tumor RNA was extracted using a RNeasy Micro Kit (Qiagen) according to the manufacturer's instructions, and gene expression was analyzed by RT-qPCR with the LightCycler 480 Real-Time PCR system (Roche Diagnostics). For cDNA synthesis, 20 ng of RNA was reverse-transcribed using the Maxima Reverse Transcriptase kit (Thermo Fisher). PCR amplification reactions were carried out in a total volume of 10 μl using SYBRGreen (Thermo Fisher). The following primers were used: CCL2—forward, 5′-CATCCACGTGTTGGCTCA-3′, reverse, 5′-GATCATCTTGCTGGTGAATGAGT-3′; CXCL9—forward, 5′-TCCTTTTGGGCATCATCTTCC-3′, reverse, 5′-TTTGTAGTGGATCGTGCCTCG-3′; and CXCL10: forward, 5-TCCTTGTCCTCCCTAGCTCA-3′, reverse, 5-ATAACCCCTTGGGAAGATGG-3′.

Cycling conditions were as follows: 94 °C for 2 min followed by 40 cycles of 15 s at 94 °C and 1 min at 60 °C. GAPDH was used as a housekeeping gene to normalize mRNA expression. Fold change in gene expression was calculated with the $2^{-\Delta\Delta Ct}$ method and normalized to the average values of the isotype-treated group. All of the measures were performed in triplicate. Raw C_t values were calculated using Lightcycler 480 v1.5.0 SP3 software.

Study Approval. Human studies were carried out according to French law on biomedical research and to principles outlined in the 1975 Helsinki Declaration and its modification. Institutional review board approval was obtained from CPP Ile de France II (#00001072, August 27, 2012).

Animal studies were approved by the animal experimentation ethics committee of Paris Descartes University (CEEA 34, 16–063).

ACKNOWLEDGMENTS. We thank Pierre Bourdoncle and Thomas Guilbert (Cochin Imaging Facility, Institut Cochin) for advice and assistance with microscopes and help in data analysis; Karine Bailly (Cochin Cytometry and Immunobiology Facility, Institut Cochin) for Luminex data acquisition; Julia Weiss for help in tumor cell transplantation; Alain Trautmann for valuable discussions and critical reading of the manuscript; Plexxikon for providing the CSF-1R inhibitors; and Robert Cardiff for providing the Met-1 tumor cell line. This study was supported by grants from the French Ligue Nationale contre le Cancer (Equipes labellisées) (to E.D.); Plan Cancer (Tumor Heterogeneity and Ecosystem Program) (to E.D.); Cancer Research for Personalized Medicine (to E.P.); Fondation de France (to E.P.); and Associazone Italiana per la Ricerca sul Cancro (to E.P.).

1. Anderson KG, Stromnes IM, Greenberg PD (2017) Obstacles posed by the tumor microenvironment to T cell activity: A case for synergistic therapies. *Cancer Cell* 31: 311–325.
2. Chen DS, Mellman I (2017) Elements of cancer immunity and the cancer-immune set point. *Nature* 541:321–330.
3. Melero I, Rouzaut A, Motz GT, Coukos G (2014) T-cell and NK-cell infiltration into solid tumors: A key limiting factor for efficacious cancer immunotherapy. *Cancer Discov* 4: 522–526.
4. Debets R, Donnadieu E, Chouaib S, Coukos G (2016) TCR-engineered T cells to treat tumors: Seeing but not touching? *Semin Immunol* 28:10–21.
5. Herbst RS, et al. (2014) Predictive correlates of response to the anti-PD-L1 antibody MPDL3280A in cancer patients. *Nature* 515:563–567.
6. Joyce JA, Fearon DT (2015) T cell exclusion, immune privilege, and the tumor microenvironment. *Science* 348:74–80.
7. Krummel MF, Bartumeus F, Gérard A (2016) T cell migration, search strategies and mechanisms. *Nat Rev Immunol* 16:193–201.
8. Weninger W, Biro M, Jain R (2014) Leukocyte migration in the interstitial space of non-lymphoid organs. *Nat Rev Immunol* 14:232–246.
9. Peranzoni E, Rivas-Caicedo A, Bougherara H, Salmon H, Donnadieu E (2013) Positive and negative influence of the matrix architecture on antitumor immune surveillance. *Cell Mol Life Sci* 70:4431–4448.
10. Bougherara H, et al. (2015) Real-time imaging of resident T cells in human lung and ovarian carcinomas reveals how different tumor microenvironments control T lymphocyte migration. *Front Immunol* 6:500.
11. Salmon H, et al. (2012) Matrix architecture defines the preferential localization and migration of T cells into the stroma of human lung tumors. *J Clin Invest* 122:899–910.
12. Feig C, et al. (2013) Targeting CXCL12 from FAP-expressing carcinoma-associated fibroblasts synergizes with anti-PD-L1 immunotherapy in pancreatic cancer. *Proc Natl Acad Sci USA* 110:20212–20217.
13. Broz ML, et al. (2014) Dissecting the tumor myeloid compartment reveals rare activating antigen-presenting cells critical for T cell immunity. *Cancer Cell* 26:638–652.
14. Engelhardt JJ, et al. (2012) Marginating dendritic cells of the tumor microenvironment cross-present tumor antigens and stably engage tumor-specific T cells. *Cancer Cell* 21:402–417.
15. Dagher NN, et al. (2015) Colony-stimulating factor 1 receptor inhibition prevents microglial plaque association and improves cognition in 3xTg-AD mice. *J Neuroinflammation* 12:139.
16. Tap WD, et al. (2015) Structure-guided blockade of CSF1R kinase in tenosynovial giant-cell tumor. *N Engl J Med* 373:428–437.
17. Borowsky AD, et al. (2005) Syngeneic mouse mammary carcinoma cell lines: Two closely related cell lines with divergent metastatic behavior. *Clin Exp Metastasis* 22: 47–59.
18. Biswas SK, Mantovani A (2010) Macrophage plasticity and interaction with lymphocyte subsets: Cancer as a paradigm. *Nat Immunol* 11:889–896.
19. Ruffell B, Coussens LM (2015) Macrophages and therapeutic resistance in cancer. *Cancer Cell* 27:462–472.
20. Mantovani A, Marchesi F, Malesci A, Laghi L, Allavena P (2017) Tumour-associated macrophages as treatment targets in oncology. *Nat Rev Clin Oncol* 14:399–416.
21. Strachan DC, et al. (2013) CSF1R inhibition delays cervical and mammary tumor growth in murine models by attenuating the turnover of tumor-associated macrophages and enhancing infiltration by $CD8^+$T cells. *Oncoimmunology* 2:e26968.
22. Zhu Y, et al. (2014) CSF1/CSF1R blockade reprograms tumor-infiltrating macrophages and improves response to T-cell checkpoint immunotherapy in pancreatic cancer models. *Cancer Res* 74:5057–5069.
23. Lesokhin AM, et al. (2012) Monocytic CCR2(+) myeloid-derived suppressor cells promote immune escape by limiting activated CD8 T-cell infiltration into the tumor microenvironment. *Cancer Res* 72:876–886.
24. Egen JG, et al. (2008) Macrophage and T cell dynamics during the development and disintegration of mycobacterial granulomas. *Immunity* 28:271–284.
25. Schläger C, et al. (2016) Effector T-cell trafficking between the leptomeninges and the cerebrospinal fluid. *Nature* 530:349–353.
26. Boissonnas A, et al. (2013) CD8+ tumor-infiltrating T cells are trapped in the tumor-dendritic cell network. *Neoplasia* 15:85–94.
27. Audemard-Verger A, et al. (2017) Macrophages induce long-term trapping of γδ T cells with innate-like properties within secondary lymphoid organs in the steady state. *J Immunol* 199:1998–2007.
28. Mikucki ME, et al. (2015) Non-redundant requirement for CXCR3 signalling during tumoricidal T-cell trafficking across tumour vascular checkpoints. *Nat Commun* 6: 7458.
29. Spranger S, Dai D, Horton B, Gajewski TF (2017) Tumor-residing Batf3 dendritic cells are required for effector T cell trafficking and adoptive T cell therapy. *Cancer Cell* 31: 711–723.e4.
30. Gordon-Alonso M, Hirsch T, Wildmann C, van der Bruggen P (2017) Galectin-3 captures interferon-gamma in the tumor matrix reducing chemokine gradient production and T-cell tumor infiltration. *Nat Commun* 8:793.
31. Afik R, et al. (2016) Tumor macrophages are pivotal constructors of tumor collagenous matrix. *J Exp Med* 213:2315–2331.
32. Tan KW, et al. (2015) Tumor stroma and chemokines control T-cell migration into melanoma following temozolomide treatment. *OncoImmunology* 4:e978709.
33. DeNardo DG, et al. (2011) Leukocyte complexity predicts breast cancer survival and functionally regulates response to chemotherapy. *Cancer Discov* 1:54–67.
34. Mok S, et al. (2014) Inhibition of CSF-1 receptor improves the antitumor efficacy of adoptive cell transfer immunotherapy. *Cancer Res* 74:153–161.
35. Boissonnas A, Fetler L, Zeelenberg IS, Hugues S, Amigorena S (2007) In vivo imaging of cytotoxic T cell infiltration and elimination of a solid tumor. *J Exp Med* 204: 345–356.
36. Deguine J, Breart B, Lemaître F, Di Santo JP, Bousso P (2010) Intravital imaging reveals distinct dynamics for natural killer and CD8(+) T cells during tumor regression. *Immunity* 33:632–644.
37. Ruocco MG, et al. (2012) Suppressing T cell motility induced by anti-CTLA-4 monotherapy improves antitumor effects. *J Clin Invest* 122:3718–3730.
38. Weigelin B, et al. (2015) Focusing and sustaining the antitumor CTL effector killer response by agonist anti-CD137 mAb. *Proc Natl Acad Sci USA* 112:7551–7556.
39. Mrass P, et al. (2006) Random migration precedes stable target cell interactions of tumor-infiltrating T cells. *J Exp Med* 203:2749–2761.
40. Fife BT, et al. (2009) Interactions between PD-1 and PD-L1 promote tolerance by blocking the TCR-induced stop signal. *Nat Immunol* 10:1185–1192.

41. Honda T, et al. (2014) Tuning of antigen sensitivity by T cell receptor-dependent negative feedback controls T cell effector function in inflamed tissues. *Immunity* 40:235–247.
42. Michonneau D, et al. (2016) The PD-1 axis enforces an anatomical segregation of CTL activity that creates tumor niches after allogeneic hematopoietic stem cell transplantation. *Immunity* 44:143–154.
43. Zinselmeyer BH, et al. (2013) PD-1 promotes immune exhaustion by inducing antiviral T cell motility paralysis. *J Exp Med* 210:757–774.
44. Hugo W, et al. (2016) Genomic and transcriptomic features of response to anti-PD-1 therapy in metastatic melanoma. *Cell* 165:35–44.
45. Wynn TA, Chawla A, Pollard JW (2013) Macrophage biology in development, homeostasis and disease. *Nature* 496:445–455.
46. Becht E, et al. (2016) Immune and stromal classification of colorectal cancer is associated with molecular subtypes and relevant for precision immunotherapy. *Clin Cancer Res* 22:4057–4066.
47. Calon A, et al. (2015) Stromal gene expression defines poor-prognosis subtypes in colorectal cancer. *Nat Genet* 47:320–329.
48. Arlauckas SP, et al. (2017) In vivo imaging reveals a tumor-associated macrophage-mediated resistance pathway in anti-PD-1 therapy. *Sci Transl Med* 9:eaal3604.
49. Cannarile MA, et al. (2017) Colony-stimulating factor 1 receptor (CSF1R) inhibitors in cancer therapy. *J Immunother Cancer* 5:53.
50. Saha D, Martuza RL, Rabkin SD (2017) Macrophage polarization contributes to glioblastoma eradication by combination immunovirotherapy and immune checkpoint blockade. *Cancer Cell* 32:253–267.e5.
51. Thoreau M, et al. (2015) Vaccine-induced tumor regression requires a dynamic cooperation between T cells and myeloid cells at the tumor site. *Oncotarget* 6: 27832–27846.
52. Long KB, Beatty GL (2013) Harnessing the antitumor potential of macrophages for cancer immunotherapy. *OncoImmunology* 2:e26860.
53. Schultze JL (2016) Reprogramming of macrophages: New opportunities for therapeutic targeting. *Curr Opin Pharmacol* 26:10–15.